Competition between spin liquids and valence-bond order in the frustrated spin-$\frac{1}{2}$ Heisenberg model on the honeycomb lattice

Francesco Ferrari,[1,*] Samuel Bieri,[2] and Federico Becca[3]

[1]*International School for Advanced Studies, Via Bonomea 265, I-34136 Trieste, Italy*
[2]*Institute for Theoretical Physics, ETH Zürich, 8099 Zürich, Switzerland*
[3]*Democritos National Simulation Center, Istituto Officina dei Materiali del CNR and International School for Advanced Studies, Via Bonomea 265, I-34136 Trieste, Italy*

Using variational wave functions and Monte Carlo techniques, we study the antiferromagnetic Heisenberg model with first-neighbor J_1 and second-neighbor J_2 antiferromagnetic couplings on the honeycomb lattice. We perform a systematic comparison of magnetically ordered and nonmagnetic states (spin liquids and valence-bond solids) to obtain the ground-state phase diagram. Néel order is stabilized for small values of the frustrating second-neighbor coupling. Increasing the ratio J_2/J_1, we find strong evidence for a continuous transition to a nonmagnetic phase at $J_2/J_1 \approx 0.23$. Close to the transition point, the Gutzwiller-projected uniform resonating valence-bond state gives an excellent approximation to the exact ground-state energy. For $0.23 \lesssim J_2/J_1 \lesssim 0.36$, a gapless Z_2 spin liquid with Dirac nodes competes with a plaquette valence-bond solid. In contrast, the gapped spin liquid considered in previous works has significantly higher variational energy. Although the plaquette valence-bond order is expected to be present as soon as the Néel order melts, this ordered state becomes clearly favored only for $J_2/J_1 \gtrsim 0.3$. Finally, for $0.36 \lesssim J_2/J_1 \leqslant 0.5$, a valence-bond solid with columnar order takes over as the ground state, being also lower in energy than the magnetic state with collinear order. We perform a detailed finite-size scaling and standard data collapse analysis, and we discuss the possibility of a deconfined quantum critical point separating the Néel antiferromagnet from the plaquette valence-bond solid.

I. INTRODUCTION

Quantum spin models on two-dimensional frustrated lattices represent important playgrounds where a variety of phases can be attained, emerging from zero-point fluctuations. Important examples include gapped and gapless spin liquids and valence-bond states [1]. Quantum fluctuations are strong when the value of the spin S on each site is small (i.e., for $S = \frac{1}{2}$) and in low spatial dimensionalities (i.e., for small coordination numbers). Furthermore, they are further enhanced in the presence of competing superexchange couplings. In this situation, long-range magnetic order can melt even at zero temperature. Then, nonmagnetic ground states can either break some symmetries (e.g., lattice translations and/or rotations), leading to a valence-bond solid (VBS), or retain all the symmetries of the Hamiltonian. In the latter case, the ground state is known as a quantum spin liquid (or quantum paramagnet). The simplest example in which the combined effect of strong quantum fluctuations and spin frustration may give rise to a magnetically disordered ground state is the J_1-J_2 Heisenberg model on the square lattice, where both first- and second-neighbor couplings are present. Here, recent numerical calculations predicted a genuine spin-liquid behavior for $J_2/J_1 \approx \frac{1}{2}$. However, it is still unclear whether the spin gap is finite, implying a topological Z_2 state, or not, thus corresponding to a critical spin liquid [2–6]. A nonmagnetic phase is expected to appear also in the J_1-J_2 model on the triangular lattice, in the vicinity of the classical transition point $J_2/J_1 \approx 1/8$. Also in this case, the nature of the ground state is not fully understood, with some calculations supporting

gapped excitations (and signatures of a spontaneously broken lattice point group) and other ones sustaining a gapless spin liquid [7–11]. Finally, a widely studied example in which the ground state does not show magnetic ordering is the Heisenberg model on the kagome lattice. Again, the true nature of the ground state is not fully understood as large-scale numerical simulations give conflicting results on the presence of a spin gap [12–16].

All these examples are characterized by an odd number of sites per unit cell, and therefore, according to the Lieb-Schultz-Mattis theorem and its generalizations [17–21], a gapped spectrum implies a degenerate ground state, either because of some symmetry breaking (leading to a VBS) or due to topological degeneracy (characteristic of Z_2 spin liquids). The honeycomb lattice, with its two sites per unit cell, represents a variation in this respect, and it may therefore show different physical properties than the previously mentioned cases. The frustrated J_1-J_2 Heisenberg model on this lattice has been investigated by a variety of analytical and numerical methods, including semiclassical [22–24], slave-particle [25,26], and variational approaches [27–29], coupled-cluster [30] and functional renormalization-group methods [31], series expansion [32], and exact diagonalization [23,33,34]. Recently, density-matrix renormalization-group (DMRG) calculations [35,36] suggested that a plaquette VBS is obtained as soon as the antiferromagnetic order melts through the frustrating superexchange coupling, i.e., for $J_2 \gtrsim 0.25J_1$. Furthermore, Ganesh *et al.* [37,38] claimed the existence of a deconfined quantum critical point, separating the Néel from the plaquette VBS phase. These DMRG results contradict earlier variational calculations that found an intermediate phase of gapped quantum spin liquid between the Néel order and the plaquette VBS [27]. This spin liquid was identified as the so-called
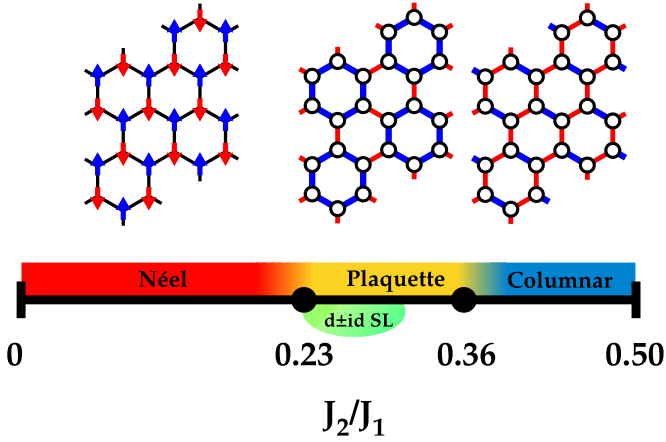
————
*frferra@sissa.it

FIG. 1. Phase diagram of the spin-$\frac{1}{2}$ J_1-J_2 Heisenberg model on the honeycomb lattice for $0 \leqslant J_2/J_1 \leqslant 0.5$ with schematic illustrations of the Néel magnetic order, plaquette, and columnar dimer orders. The solid dots indicate quantum phase transitions between Néel and plaquette VBS ($J_2/J_1 \approx 0.23$) and between plaquette and columnar VBS ($J_2/J_1 \approx 0.36$). The region where the $d \pm id$ spin liquid has a competitive energy is marked by the green oval.

FIG. 2. The honeycomb lattice is shown on the left: $\mathbf{a}_1$ and $\mathbf{a}_2$ are the primitive vectors of the Bravais lattice. A and B denote the two sublattices: A-type sites are placed at the origin of the unit cell, while B-type sites are displaced by $(0,1)$. The dashed lines represent the directions of the vectors $\mathbf{T}_1$ and $\mathbf{T}_2$ that define the finite lattice clusters used in the calculations. A schematic illustration of the interactions in the J_1-J_2 Heisenberg model is shown on the right.

sublattice pairing state (SPS) [26,36,39]. The SPS was originally motivated by the idea that the half-filled Hubbard model on the honeycomb lattice could sustain a gapped spin-liquid phase at intermediate values of electron-electron repulsion [40]. However, this idea eventually turned out to be incorrect [41].

In this paper, we revisit the ground-state phase diagram of the spin-$\frac{1}{2}$ J_1-J_2 Heisenberg model on the honeycomb lattice using variational wave functions that can describe both magnetically ordered and disordered phases. As far as the latter are concerned, we perform a systematic study of all possible spin-liquid *Ansätze* that have been classified in Ref. [26], including chiral states as well. Moreover, we construct VBS wave functions that are compatible with the previous DMRG simulations (including both plaquette and columnar orders). Our results show that the Néel order melts for $J_2/J_1 \approx 0.23$, in very good agreement with DMRG [35,36,38]. Furthermore, we find that the best spin-liquid wave function for $J_2/J_1 \gtrsim 0.23$ is not the gapped SPS as claimed earlier [27,36] but instead a symmetric Z_2 state with Dirac cones (which is dubbed $d \pm id$), distinct from all previously discussed spin-liquid phases. Nonetheless, for $J_2/J_1 \gtrsim 0.3$ we find a substantial energy gain when translation symmetry is broken in the variational *Ansatz*, suggesting the presence of a plaquette VBS as soon as the Néel order melts through spin frustration. Our finite-size scaling analysis supports the conclusion of a continuous Néel to VBS transition and may be consistent with the presence of a quantum critical point. For even stronger frustration (i.e., $J_2/J_1 \gtrsim 0.36$), a VBS with columnar dimers becomes energetically favored. A sketch of the quantum phase diagram is shown in Fig. 1.

This paper is organized as follows: In Sec. II we give details of the model and the variational wave functions that have been employed. In Sec. III, we show the numerical results, and, finally, in Sec. IV, we draw our conclusions.
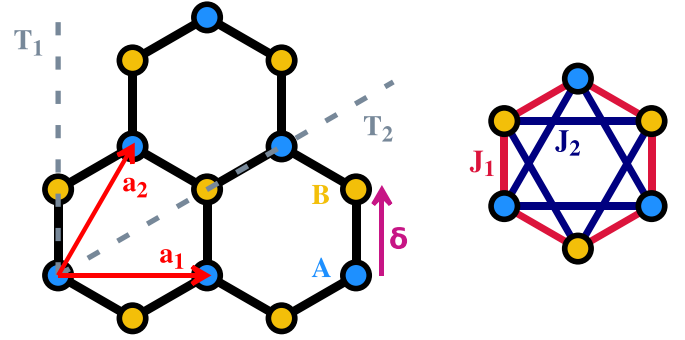
II. MODEL AND METHODS

The spin-$\frac{1}{2}$ J_1-J_2 Heisenberg model is defined by

$$\mathcal{H} = J_1 \sum_{\langle i,j \rangle} \mathbf{S}_i \cdot \mathbf{S}_j + J_2 \sum_{\langle\langle i,j \rangle\rangle} \mathbf{S}_i \cdot \mathbf{S}_j, \tag{1}$$

where $\langle i,j \rangle$ and $\langle\langle i,j \rangle\rangle$ denote first- and second-neighbor bonds, respectively (see Fig. 2). The honeycomb lattice has two sites per unit cell, and the underlying Bravais lattice has a triangular structure with primitive vectors $\mathbf{a}_1 = (\sqrt{3},0)$ and $\mathbf{a}_2 = (\sqrt{3}/2,3/2)$. The two sites in the unit cell are labeled by A and B: the former one is placed in the origin of the cell, while the latter one is displaced by the unit vector $\boldsymbol{\delta} = (0,1)$ (see Fig. 2). Then, the coordinates of the site i are given by $\mathbf{R}_i = \mathbf{R}_i^0 + \eta_i \boldsymbol{\delta}$, where $\mathbf{R}_i^0 = n_i \mathbf{a}_1 + m_i \mathbf{a}_2$, with n_i and m_i being integers and the two sites in the unit cell having the same $\mathbf{R}_i^0$ and $\eta_i = 0$ or 1. Note that our choice of primitive vectors is such that the first-neighbor distance is equal to 1. For our numerical calculations, we take lattice clusters that are defined by $\mathbf{T}_1 = 2L\mathbf{a}_2 - L\mathbf{a}_1$ and $\mathbf{T}_2 = L\mathbf{a}_2 + L\mathbf{a}_1$, thus consisting of $N_s = 6L^2$ sites (i.e., $3L^2$ unit cells with two sites each). Periodic boundary conditions are imposed on the spin model of Eq. (1).

Our results are obtained using variational wave functions constructed from so-called Gutzwiller-projected fermionic states defined as

$$|\Psi\rangle = \mathcal{P}_{S_z^{\text{tot}}} \mathcal{J}_z \mathcal{P}_G |\Phi_0\rangle. \tag{2}$$

Here, $|\Phi_0\rangle$ is the ground state of suitable quadratic Hamiltonians for auxiliary spinful fermions $\{c_{i,\uparrow}, c_{i,\downarrow}\}$ described below. $\mathcal{P}_G = \prod_i (n_{i,\uparrow} - n_{i,\downarrow})^2$ is the Gutzwiller projector that enforces exactly one fermion per site ($n_{i,\sigma} = c_{i,\sigma}^\dagger c_{i,\sigma}$), which is needed in order to obtain a faithful wave function for the Heisenberg model. $\mathcal{P}_{S_z^{\text{tot}}}$ is the projector on the subspace in which the z component of the total spin is zero. Finally, $\mathcal{J}_z$ is the spin-spin Jastrow factor:

$$\mathcal{J}_z = \exp\left(-\frac{1}{2} \sum_{i,j} v_{ij} S_i^z S_j^z\right), \tag{3}$$

where the pseudopotential v_{ij} depends on the distance $|\mathbf{R}_i - \mathbf{R}_j|$ (for a translationally invariant system).

Let us now describe in detail the form of the quadratic Hamiltonians that are used to define $|\Phi_0\rangle$. We will mainly consider two options: one for magnetically ordered phases and the other for nonmagnetic phases. In the first case, we take

$$\mathcal{H}_{\mathrm{mag}} = \sum_{i,j,\sigma} t_{ij} c_{i,\sigma}^\dagger c_{j,\sigma} + \mathrm{H.c.} + \sum_i h_i(c_{i,\uparrow}^\dagger c_{i,\downarrow} + c_{i,\downarrow}^\dagger c_{i,\uparrow}),$$
(4)

where t_{ij} denotes the hopping amplitude and h_i is a (fictitious) magnetic field along the x direction, which is taken to have a periodic pattern:

$$h_j = h \exp[i(\mathbf{Q} \cdot \mathbf{R}_j^0 + \phi_j)],$$
(5)

where $\mathbf{Q}$ is the wave vector that fixes the periodicity and ϕ_j is a sublattice-dependent phase shift. In this work, we consider the antiferromagnetic Néel phase with $\mathbf{Q} = (0,0)$ and $\phi_j = \eta_j \pi$ (i.e., $\phi_j = 0$ for $j \in A$ and $\phi_j = \pi$ for $j \in B$) and a collinear phase with $\mathbf{Q} = (0, 2\pi/3)$ and $\phi_i = 0$. Within this kind of magnetically ordered states, it is very important to take into account the spin-spin Jastrow factor in order to introduce transverse spin fluctuations (i.e., spin waves) [42]. We mention in passing that the case $t_{ij} = 0$ reduces to a "bosonic" (pure Jastrow) state, which has been used by Di Ciolo *et al.* for this model [29]. Interestingly, we find that a nonzero uniform first-neighbor hopping *does* provide an energy gain with respect to this "bosonic" case. This situation is similar to the triangular-lattice antiferromagnet, where a hopping term with Dirac spectrum was also found to result in a substantial energy gain [11].

In contrast, nonmagnetic phases, such as spin liquids and VBSs, can be described by taking

$$\mathcal{H}_{\mathrm{sl}} = \sum_{i,j,\sigma} t_{ij} c_{i,\sigma}^\dagger c_{j,\sigma} + \sum_{ij} \Delta_{ij} c_{i,\downarrow} c_{j,\uparrow} + \mathrm{H.c.}$$
$$+ \sum_{i,\sigma} \mu_i c_{i,\sigma}^\dagger c_{i,\sigma} + \sum_i \zeta_i c_{i,\downarrow} c_{i,\uparrow} + \mathrm{H.c.},$$
(6)

where, in addition to the hopping, we introduce singlet pairing terms, ζ_i and $\Delta_{ij} = \Delta_{ji}$, as well as a chemical potential μ_i. Within this framework, a classification of distinct spin-liquid phases can be obtained through the so-called projective-symmetry-group (PSG) analysis [43,44]. From a variational perspective, the PSG provides a recipe for constructing symmetric spin-liquid wave functions through specific *Ansätze* for the Hamiltonian (6). The simplest *Ansatz* is given by a first-neighbor hopping ($t_{ij} = t$) and no pairing terms ($\Delta_{ij} = \zeta_i = 0$). This is the *uniform resonating valence-bond* (uRVB) state, which is a U(1) state with Dirac cones at the corners of the hexagonal Brillouin zone. By performing a PSG classification, Lu and Ran [26] found 24 symmetric Z_2 spin liquids that are continuously connected to this uRVB (i.e., that can be obtained from the uRVB by adding further hopping and/or pairing terms). Among those states, the presence of the gapped SPS was emphasized. The SPS *Ansatz* is characterized by a uniform first-neighbor hopping t and a complex second-neighbor pairing with opposite phases on A-A and B-B links, i.e., $\Delta_{ij}^{AA} = \Delta e^{i\theta}$ and $\Delta_{ij}^{BB} = \Delta e^{-i\theta}$. Such a state is always gapped if $\Delta \neq 0$ and $\theta \neq \pi/2$. In principle, the PSG classification
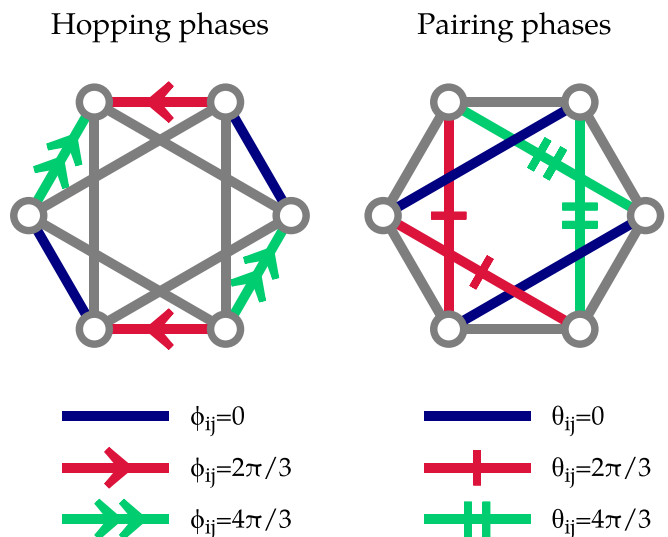

FIG. 3. Schematic illustration of the $d \pm id$ spin-liquid state. Here, ϕ_{ij} and θ_{ij} are the complex phases of first-neighbor hopping and second-neighbor pairing, respectively. The direction of the arrows ($i \rightarrow j$) indicates the convention of phases for the hopping terms.

also allows an on-site pairing with opposite phases on the two sublattices, i.e., $\zeta_i^A = \zeta e^{i\phi}$, $\zeta_i^B = \zeta e^{-i\phi}$. In agreement with previous studies [27,36], we find that the SPS *Ansatz* has a lower variational energy than the uRVB state for $J_2/J_1 \gtrsim 0.25$. The actual value of θ can be set to zero since the variational energy does not change appreciably for $\theta \lesssim \pi/4$. However, here, we find another *gapless* spin liquid (i.e., number 18 in Table I of Ref. [26]) that has an even lower energy than the SPS wave function and represents the best Z_2 state among those classified within the fermionic PSG. We adopt a natural gauge in which this spin-liquid *Ansatz* has first-neighbor hopping $t_{ij} = te^{i\phi_{ij}}$ and second-neighbor pairing $\Delta_{ij} = \Delta e^{i\theta_{ij}}$ with complex phases as given in Fig. 3, a convention that differs from the original PSG solution of Ref. [26]. Since Δ_{ij} has a $d_{x^2-y^2} + id_{xy}$ phase winding on the triangular lattice of A sites and $d_{x^2-y^2} - id_{xy}$ on the B sublattice, we call this new state $d \pm id$. For $\Delta = 0$, the $d \pm id$ state reduces to uRVB, while for $t = 0$, it is two copies of the *quadratic band touching* state that has been discussed in Ref. [7] for the triangular lattice. For finite Δ, the fermionic mean-field energy bands show Dirac nodes at the center and at the corners of the Brillouin zone (see Fig. 4). Note that, despite the presence of complex hopping and pairing terms, both the SPS and the $d \pm id$ states do not break time-reversal symmetry (or any other lattice symmetry) once the wave function is Gutzwiller projected to the physical spin Hilbert space (see the Appendix for its projective symmetries). Beyond fully symmetric phases, we also looked for potential chiral spin liquids as outlined in Ref. [44]. However, we do not find any indication for such ground states in the present model.

Using the Hamiltonian of Eq. (6), we can also construct wave functions with VBS order. This can be achieved by allowing a translation and/or rotation symmetry breaking in the hopping t_{ij} and/or in the pairing Δ_{ij} parameters. Here, we consider two possibilities which are motivated by recent DMRG results [35,36,38]. These are obtained by considering
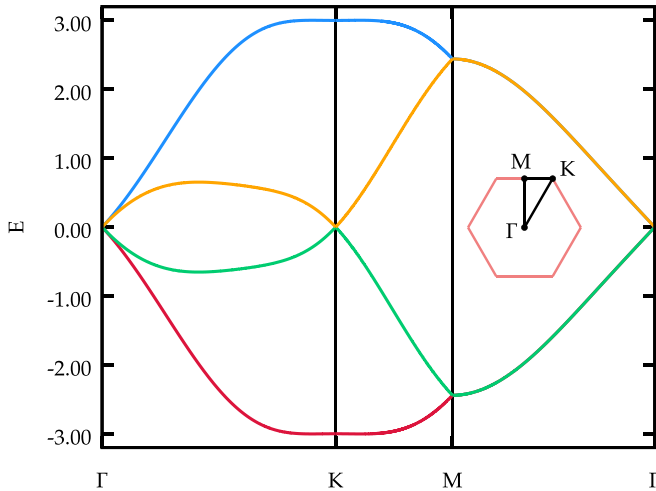
FIG. 4. Mean-field spectrum of the gapless $d \pm id$ pairing state. The energy bands are shown along the path $\Gamma \rightarrow K \rightarrow M \rightarrow \Gamma$ in the Brillouin zone (inset). The value of the second-neighbor pairing is $\Delta = 0.35t$, which is very close to the optimal value obtained for $J_2/J_1 = 0.35$. The bands show Dirac cones located at Γ and K points. Note that the two bands are twice degenerate along $M \rightarrow \Gamma$.

two different first-neighbor hoppings t and t', forming "strong" and "weak" plaquettes or columnar dimers (see Fig. 5). In both cases, a remarkable improvement in variational energy is achieved by adding a (uniform) second-neighbor pairing with $d \pm id$ symmetry, as well as including the corresponding complex phases for the dimerized first-neighbor hoppings (Fig. 3). These are rare examples of clear VBS instabilities in frustrated two-dimensional Heisenberg models using Peierls-type mean-field parameters in Gutzwiller-projected wave functions (see, e.g., Ref. [45]).

Finally, we would like to emphasize that, in order to calculate observables (e.g., the variational energy or any correlation function) in the state of Eq. (2), Monte Carlo sampling is needed since an analytic treatment is not possible in two spatial dimensions. The optimal variational parameters (including the ones defining the quadratic Hamiltonian and the Jastrow pseudopotential) for each value of the ratio J_2/J_1 can be obtained using the stochastic reconfiguration technique [46].
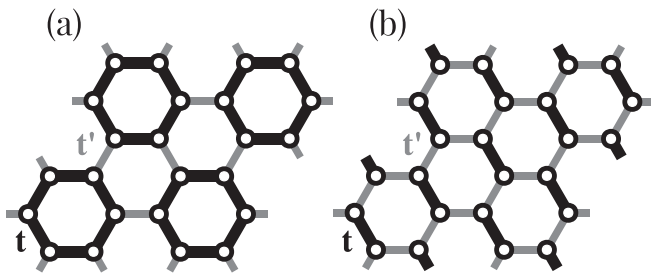

FIG. 5. Patterns of the first-neighbor hoppings in the quadratic Hamiltonian (6) as found (a) in the plaquette VBS and (b) in the columnar VBS.

III. RESULTS

In the following, we show the numerical results obtained with the variational approach described in the previous section.

A. Accuracy of the wave functions

Let us first discuss the accuracy of the optimized variational energy for various states on a small lattice cluster with 24 sites (i.e., $L = 2$) for which exact diagonalization is available. In Fig. 6, we present the results for the uRVB state (with only first-neighbor hopping), the Néel state (also including the fictitious magnetic field h_i and the spin-spin Jastrow factor), the SPS *Ansatz* (with second-neighbor pairing and $\theta = 0$), and the $d \pm id$ state. First of all, starting from the unfrustrated limit with $J_2 = 0$, the accuracy of the uRVB state clearly improves until $J_2/J_1 \approx 0.2$. Then the energy rapidly deteriorates when J_2/J_1 is further increased. For $J_2/J_1 \lesssim 0.2$, the best variational state is given by including Néel order with $\mathbf{Q} = (0,0)$ and $\phi_i = \eta_i \pi$. In this regime, the strength of the magnetic field h in Eq. (5) decreases as J_2/J_1 increases, and it goes to zero for $J_2/J_1 \gtrsim 0.2$. When $h = 0$, only a marginal energy gain with respect to the uRVB state is obtained due to a (small) spin-spin Jastrow factor. For this reason, the results for the Néel state are not reported for $J_2/J_1 > 0.2$. In contrast, an energy gain is found in this regime by allowing a pairing term in Eq. (6). Here, both the SPS and the $d \pm id$ *Ansätze* give a lower variational energy than the simple uRVB. We emphasize that the $d \pm id$ wave function represents the best fermionic state among the 24 Z_2 spin liquids listed in Ref. [26]. On the small cluster considered, there is no significant energy gain by allowing VBS order on top of the $d \pm id$ state for $J_2/J_1 \lesssim 0.35$.

B. The Néel phase

In order to draw the ground-state phase diagram, we focus on the Néel phase and perform a finite-size scaling of the
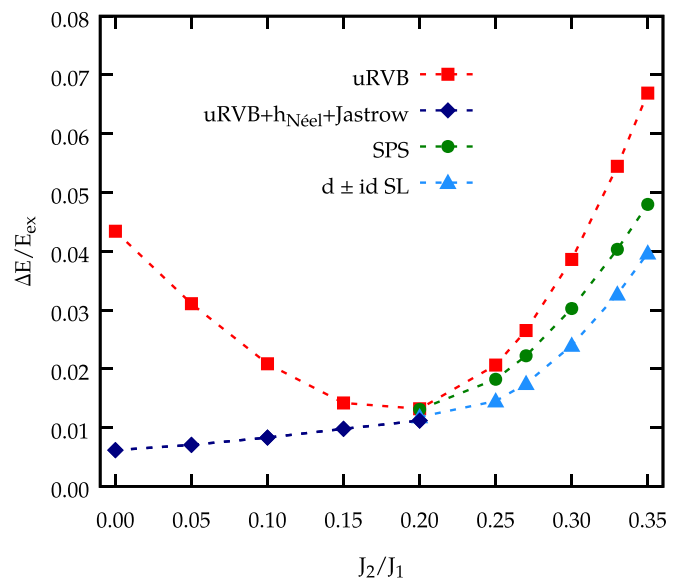

FIG. 6. Accuracy of the variational energy for different wave functions on the 24-site cluster. Here, ΔE is the difference between the variational (E_{var}) and the exact (E_{ex}) ground-state energy.
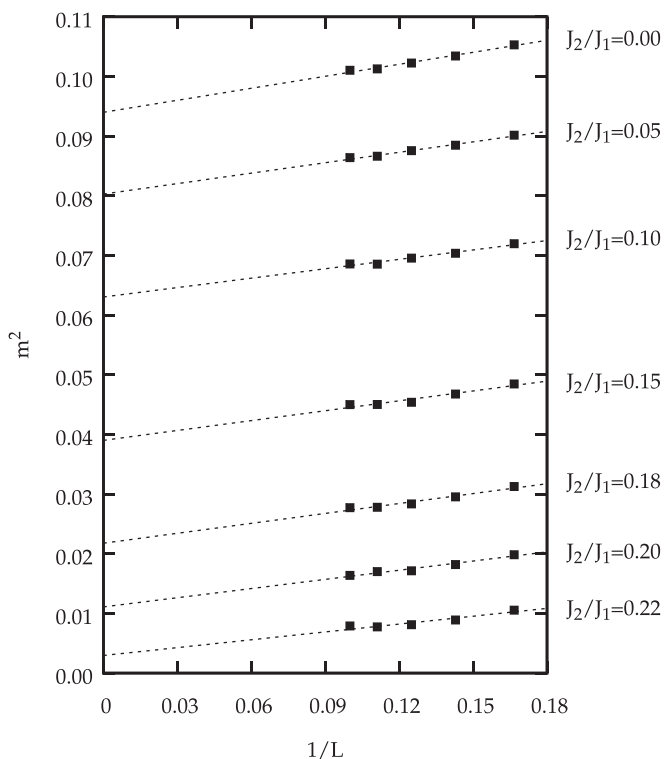
FIG. 7. Finite-size scaling of the square magnetization m^2, Eq. (7), for different values of J_2/J_1. For $J_2 = 0$ the optimal value of the fictitious magnetic field is $h/t \approx 0.32$.

magnetization, which is obtained from the expectation value of the spin-spin correlation at the maximal distance

$$m^2 = \lim_{|i-j| \to \infty} \langle \mathbf{S}_i \cdot \mathbf{S}_j \rangle \qquad (7)$$

in the variational state $|\Psi\rangle$. The results for $0 \leqslant J_2/J_1 \leqslant 0.22$ are reported in Fig. 7 for L ranging from 6 to 10 (i.e., up to 600 sites). The thermodynamic extrapolation of the magnetization m is shown in Fig. 8. The expected $1/L$ corrections are
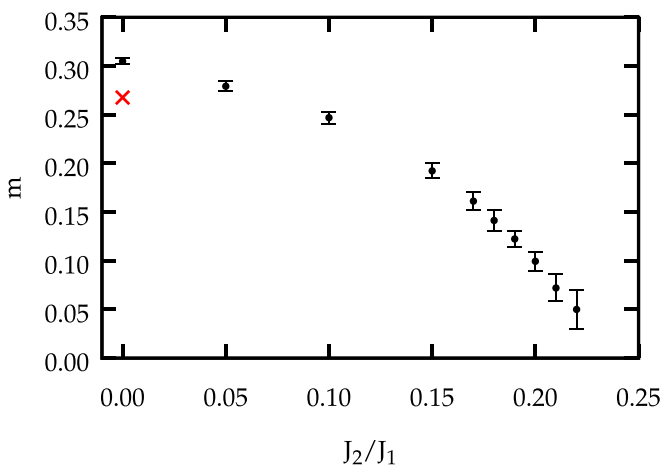

FIG. 8. Thermodynamic limit of the magnetization m as a function of J_2/J_1. The result from quantum Monte Carlo of Ref. [47] for $J_2 = 0$ is shown for comparison (red cross). The classical value is $m = 0.5$.

correctly reproduced by the spin-spin Jastrow factor, which is able to introduce the relevant low-energy fluctuations on top of the classical order parameter that is generated by the magnetic field h of Eq. (5). The thermodynamic value of the staggered magnetization vanishes for $J_2/J_1 \approx 0.23$ (see also the discussion in Sec. IV), in good agreement with previous DMRG calculations [35,36,38]. We remark that the value $J_2/J_1 \approx 0.23$ is larger than the one obtained in the classical limit (i.e., $J_2/J_1 = 1/6$), indicating that quantum fluctuations favor collinear magnetic order over generic coplanar spirals (which represent the classical ground state for $J_2/J_1 > 1/6$). Comparison with exact quantum Monte Carlo calculations, which are possible only in the unfrustrated case $J_2 = 0$ [47], further substantiates the accuracy of the Néel wave function on large systems (see Fig. 8). Even though a direct inspection of our numerical results cannot exclude a first-order transition at $J_2/J_1 \approx 0.23$, a detailed finite-size scaling analysis based on data collapse suggests that the transition between the Néel and nonmagnetic phase is continuous (see below).

C. The nonmagnetic phase

Increasing the ratio J_2/J_1, the Néel order melts, and the natural expectation is that a nonmagnetic phase is stabilized by quantum fluctuations. Nonetheless, we cannot exclude that magnetic states with *incommensurate* spirals are favored instead, which occurs in the classical limit for $J_2/J_1 > 1/6$. In any numerical calculation that considers finite clusters, it is very difficult to assess states with large periodicity or with pitch vectors that are not allowed by the finite-cluster geometry. Therefore, we will not consider the possibility of incommensurate spiral orders here, and we restrict ourselves to states with collinear order, i.e., the one with $\mathbf{Q} = (0, 2\pi/3)$ and $\phi_i = 0$. This restriction is justified by recent variational Monte Carlo results showing that collinear states (or short-period spirals) may prevail over generic states with long periodicity [29]. As far as the nonmagnetic states are concerned, we consider the ones that can be constructed with the help of the Hamiltonian (6). For these cases, we do not include the spin-spin Jastrow factor (3) since this term would break SU(2) spin-rotation symmetry (in any case, the inclusion of a Jastrow factor leads to only minor energy gains).

In Fig. 9, we report the finite-size scaling of the energies for $J_2/J_1 = 0.3, 0.35,$ and 0.4. Various variational wave functions are reported since the uRVB is unstable when adding pairing terms or allowing a translation symmetry breaking in the quadratic Hamiltonian. First of all, the SPS *Ansatz* gives a size-consistent improvement with respect to the uRVB state in both cases. Our calculations are shown for $\theta = 0$. In addition to the second-neighbor pairing, the symmetry-allowed nonzero on-site pairing leads to a *gapless* mean-field spectrum, spoiling the gapped nature of the SPS *Ansatz*. However, this variational freedom does not give an appreciable energy gain for the values of J_2/J_1 considered here. The best spin-liquid wave function, among the 24 possibilities listed in Ref. [26], is the $d \pm id$ state discussed in Sec. II. But most strikingly, the lowest-energy state in this regime has plaquette VBS order, where the first-neighbor hoppings exhibit the pattern shown in Fig. 5(a). Here, the presence of a second-neighbor pairing with $d \pm id$ symmetry gives a significant improvement
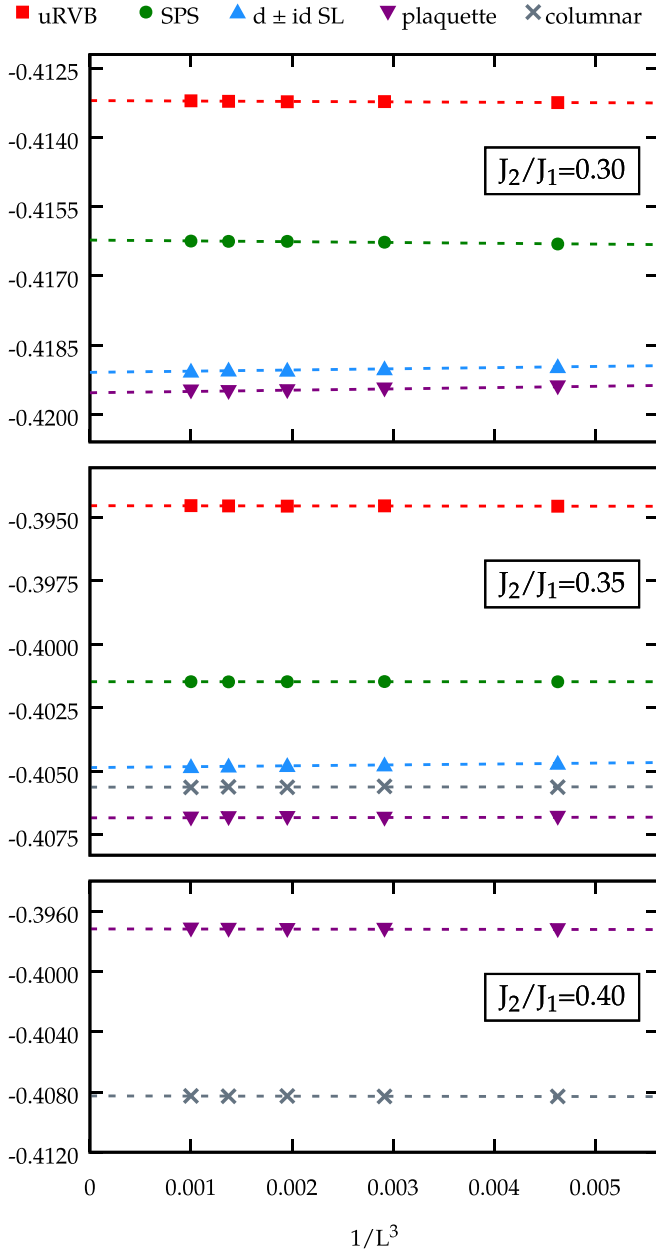
FIG. 9. Finite-size scaling analysis of the variational energy of different wave functions for $J_2/J_1 = 0.3$, 0.35, and 0.4. Statistical errors are smaller than the symbol size. The uRVB, SPS, and $d \pm id$ states are reported only for $J_2/J_1 = 0.3$ and 0.35; for $J_2/J_1 = 0.4$, their energies are much higher than those of plaquette and columnar dimer VBS states. The dashed lines are the fitting functions used for the extrapolation to the thermodynamic limit. For the $d \pm id$ state, the optimal values of the parameters are $\Delta/t \approx 0.31$ and $\Delta/t \approx 0.36$ for $J_2/J_1 = 0.3$ and 0.35, respectively. For the plaquette state the parameters range from $\Delta/t \approx 0.31$ and $t'/t \approx 0.90$ for $J_2/J_1 = 0.3$ to $\Delta/t \approx 0.38$ and $t'/t \approx 0.62$ for $J_2/J_1 = 0.4$. Finally, for the columnar state we get $\Delta/t \approx 0.34$ ($\Delta/t \approx 0.37$) and $t'/t \approx 0.45$ ($t'/t \approx 0.20$) for $J_2/J_1 = 0.35$ ($J_2/J_1 = 0.4$).

in the variational energy, but the stabilization of a plaquette state is already observed using only first-neighbor hopping. Its energy gain with respect to the uniform $d \pm id$ *Ansatz* clearly increases with increasing J_2/J_1, being approximately
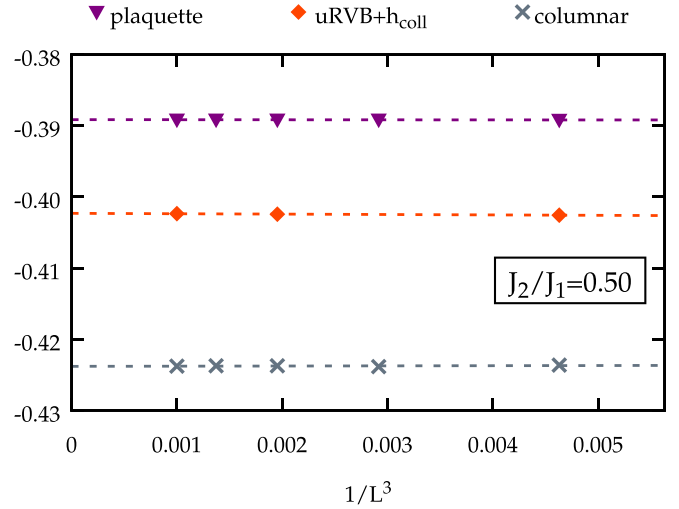

FIG. 10. Finite-size scaling analysis of the variational energy of VBS and collinear magnetic states at $J_2/J_1 = 0.5$. The optimal values for the plaquette state are $\Delta/t \approx 0.40$ and $t'/t \approx 0.20$. For the columnar state t'/t is essentially zero, while $\Delta/t \approx 0.37$. The fictitious magnetic field of the collinear state has optimal value $h/t \approx 0.98$.

$5 \times 10^{-4} J_1$ for $J_2/J_1 = 0.3$ and $2 \times 10^{-3} J_1$ for $J_2/J_1 = 0.35$ (see Fig. 9).

Further increasing J_2/J_1, a different VBS with columnar order wins over the plaquette VBS (see Fig. 9). The corresponding pattern of first-neighbor hoppings is shown in Fig. 5(b). Again, a second-neighbor $d \pm id$ pairing gives a substantial energy gain, allowing us to obtain a stable optimization of the columnar order. The fact that both columnar and plaquette states can be stabilized, even when their respective energy is higher than that of the competitor, strongly suggests that the transition between these two VBS phases is first order. Based on the calculation of variational energies on relatively large clusters, our estimation of the transition point is $J_2/J_1 \approx 0.36$ (in remarkably good agreement with DMRG [35,38]).

Finally, we briefly discuss the possible emergence of magnetic order close to $J_2/J_1 = 0.5$. Unfortunately, the pitch vector of the relevant magnetic state that is found at the classical and semiclassical levels varies continuously with J_2/J_1 [23,24]. This fact makes it impossible to determine the best spiral state on finite clusters. However, for $J_2/J_1 = 0.5$, the classical state that is selected by quantum fluctuations is relatively simple, having collinear order. More specifically, it has spins that are antiferromagnetically aligned on two out of the three first-neighbor directions and ferromagnetically aligned on the third direction. There are three inequivalent possibilities for this ordering (corresponding to the choice of the ferromagnetic bond), and therefore, this state breaks rotation symmetry (similar to the J_1-J_2 model on the square lattice for $J_2/J_1 > 0.5$ [48]). In the following, we compare the VBS and the collinear magnetic state for $J_2/J_1 = 0.45$ and 0.5. We take the best VBS *Ansatz*, which is given by the columnar state (including the $d \pm id$ pairing), and a magnetically ordered wave function, which is constructed using Eq. (4) with $\mathbf{Q} = (0, 2\pi/3)$ and $\phi_i = 0$. The results of the finite-size scaling of the energies are shown in Fig. 10 for

$J_2/J_1 = 0.5$ (similar results are obtained for $J_2/J_1 = 0.45$). In this regime, the VBS *Ansatz* overcomes the collinear state with a remarkable energy gain. Therefore, we can safely affirm that, for $0.36 \lesssim J_2/J_1 \leqslant 0.5$, the best variational wave function exhibits VBS order. These results are in agreement with previous studies [27,38], which detected signatures of rotation symmetry breaking and suggested the existence of a dimerized phase for large values of J_2/J_1.

D. Néel to VBS transition: Finite-size scaling analysis

In this section, we briefly discuss the possibility for the Néel to VBS transition to be an example of the so-called *deconfined quantum criticality* [49,50] as suggested by Ganesh *et al.* [37,38]. We compute both the magnetization [see Eq. (7)] and the VBS order parameter:

$$\psi = \frac{1}{N} \sum_{i \in A} \langle D_i \rangle e^{-i \frac{2\pi}{3}(n_i - m_i)}, \tag{8}$$

where

$$D_i = S_i^z S_{i+x}^z + S_i^z S_{i+y}^z e^{i\frac{2\pi}{3}} + S_i^z S_{i+z}^z e^{-i\frac{2\pi}{3}}. \tag{9}$$

Here, site i has coordinates $\mathbf{R}_i = n_i \mathbf{a}_1 + m_i \mathbf{a}_2$ (belonging to sublattice A), while sites $i+x$, $i+y$, and $i+z$ have coordinates $\mathbf{R}_i - \mathbf{a}_2 + \boldsymbol{\delta}$, $\mathbf{R}_i + \mathbf{a}_1 - \mathbf{a}_2 + \boldsymbol{\delta}$, and $\mathbf{R}_i + \boldsymbol{\delta}$, respectively [51]. Note that, since the variational wave function explicitly breaks translation symmetry, the order parameter (and not its square) can be directly assessed in the numerical calculation. For continuous transitions, we have

$$m^2 L^{1+\eta_m} = F_m\left[\left(\frac{J_2 - J_{cm}}{J_{cm}}\right)L^{1/\nu_m}\right], \tag{10}$$

$$|\psi|^2 L^{1+\eta_p} = F_p\left[\left(\frac{J_2 - J_{cp}}{J_{cp}}\right)L^{1/\nu_p}\right], \tag{11}$$

where ν_m (ν_p) is the exponent for the magnetic (plaquette) correlation length, η_m (η_p) is the exponent for this correlation function at criticality, and J_{cm} and J_{cp} are the values of J_2 at the transition points. Finally, F_m and F_p are suitable scaling functions. In the case of deconfined criticality, we must have $J_{cm} = J_{cp}$ and $\nu_m = \nu_p$, while the exponents are different, i.e., $\eta_m \neq \eta_p$. The results for the magnetization m^2 and for the plaquette order $|\psi|^2$ are reported in Fig. 11. Performing two separate fitting procedures based on a Bayesian statistical analysis [52], we get $J_{cm} = 0.234(1)$, $\nu_m = 0.664(1)$, $\eta_m = 0.837(1)$ for the magnetization and $J_{cp} = 0.224(1)$, $\nu_p = 1.077(1)$, $\eta_p = 0.799(1)$ for the plaquette order. These fitting procedures give a remarkably good collapse of the two curves. Note that the evaluations of the critical points are in very good agreement, and also the values of η_s and η_p may be compatible with the prediction of the theory [53]. However, the values of the exponents ν_m and ν_p are quite different, with an anomalously large value obtained for $|\psi|^2$. In fact, when attempting to fit both curves with the same ν, a much worse result is obtained (not shown), and the data collapsing procedure fails in a large part of the magnetization curve.

When analyzing these scaling results, one must keep in mind that they are obtained within a variational approach, which may miss subtle details of the final phase diagram. Therefore, it can be very difficult to detect the existence of
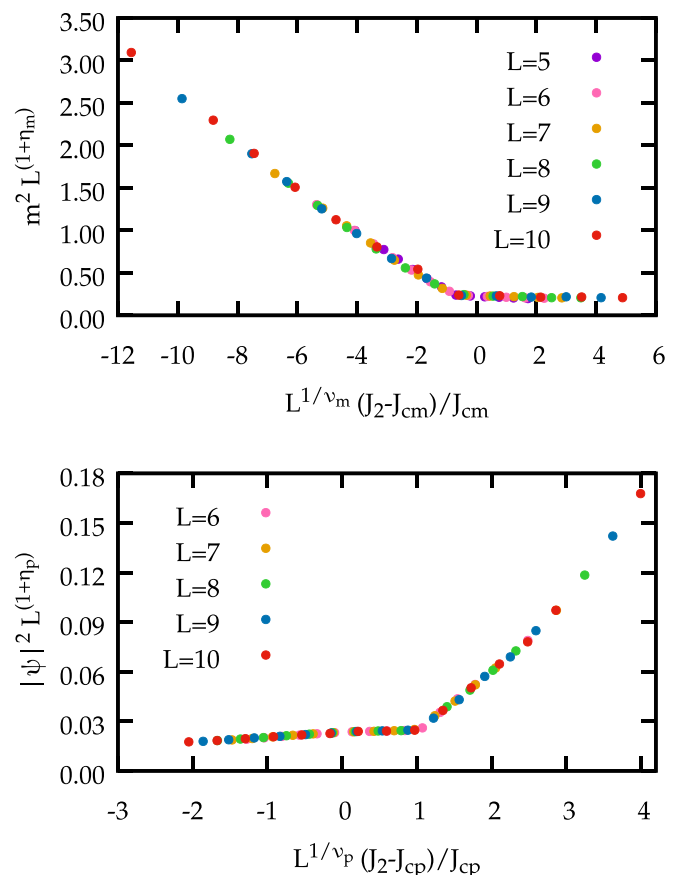

FIG. 11. Finite-size scaling collapse of the data of the antiferromagnetic (top) and plaquette (bottom) order parameters.

a deconfined quantum criticality. Nevertheless, it is striking that the two transitions look continuous with critical values J_c that are extremely close to each other. The failure to obtain a good collapse with a single exponent ν could be due to the approximate nature of the variational wave function, which may not be particularly accurate in the VBS region (see Fig. 6).

IV. CONCLUSIONS

In conclusion, we have employed variational wave functions and quantum Monte Carlo methods to study the frustrated J_1-J_2 Heisenberg model on the honeycomb lattice. We find that quantum fluctuations enlarge the region of stability of the collinear Néel phase with respect to the classical model, up to $J_2/J_1 \approx 0.23$. Further increasing J_2/J_1, a plaquette VBS order is stabilized, even though a gapless Z_2 spin liquid (dubbed $d \pm id$) represents a state with highly competitive variational energy, especially in the proximity of the phase transition. We expect that this interesting new spin liquid can possibly be favored by farther-range couplings or by ring-exchange terms. At $J_2/J_1 \approx 0.36$, another VBS state with columnar order becomes energetically favored. Our results are in excellent agreement with recent DMRG calculations [35,36,38].

Regarding the nature of the Néel to VBS transition, we hope that the promising results obtained by our approach will give new impetus to examine the topic of a deconfined

quantum critical point in the frustrated Heisenberg model on the honeycomb lattice.

APPENDIX: PSG OF THE $d \pm id$ SPIN LIQUID

In this appendix, we briefly discuss the projective symmetry group [43,44] and some physical properties of the competitive $d \pm id$ state discussed in this paper. For this purpose, we introduce a different formulation of the Hamiltonian of Eq. (6), dropping the on-site terms which are not relevant for the present discussion:

$$\mathcal{H}_{sl} = \sum_{i,j} \psi_i^\dagger u_{ij} \psi_j = \sum_{i,j} (c_{i,\uparrow}^\dagger, c_{i,\downarrow}) \begin{pmatrix} t_{ij} & \Delta_{ij}^* \\ \Delta_{ij} & -t_{ij}^* \end{pmatrix} \begin{pmatrix} c_{j,\uparrow} \\ c_{j,\downarrow}^\dagger \end{pmatrix}.$$
(A1)

A spin-liquid *Ansatz* u_{ij} is invariant under the combined effect of a lattice symmetry transformation $\mathcal{O}$ and the corresponding gauge transformation $g_{\mathcal{O}}$, namely,

$$u_{ij} = g_{\mathcal{O}}(i) u_{\mathcal{O}^{-1}(i)\mathcal{O}^{-1}(j)} g_{\mathcal{O}}^\dagger(j).$$
(A2)

The $d \pm id$ spin-liquid state is classified as number 18 in Table I of Ref. [26]. In the gauge employed in that paper, the quadratic mean-field Hamiltonian has a large cell (i.e., six sites). Here, we use a more natural gauge where the unit cell of the honeycomb lattice is not enlarged. In our gauge, both first-neighbor hopping phases and second-neighbor pairing phases undergo a $l = 2$ phase winding, as shown in Fig. 3. As a trade-off for the simplicity of the *Ansatz*, the projective representation of symmetries is slightly more involved in this gauge.

More explicitly, in our gauge we have trivial representations of lattice translations along $\mathbf{a}_1$ and $\mathbf{a}_2$, namely, $g_1 = g_2 = \mathbb{1}_2$. The projective representation of the point-group symmetries, i.e., the mirror reflection σ and the sixfold rotation R (see Fig. 12), is the following:

$$g_\sigma(s) = \mathbb{1}_2,$$
(A3)

$$g_R(s) = (-)^s i\sigma_1 e^{(1-2s)\frac{\pi}{3}i\sigma_3},$$
(A4)

where $s = 0,1$ is the sublattice index. Finally, for the time reversal T, we have

$$g_T(s) = (-)^s i\sigma_3.$$
(A5)

For example, Eq. (A5) implies that complex hopping terms between sites of different sublattices and complex pairing terms between sites of the same sublattice are time reversal invariant [44]. The gauge transformation that relates our gauge for the $d \pm id$ state to the one used in Ref. [26] (number 18 in
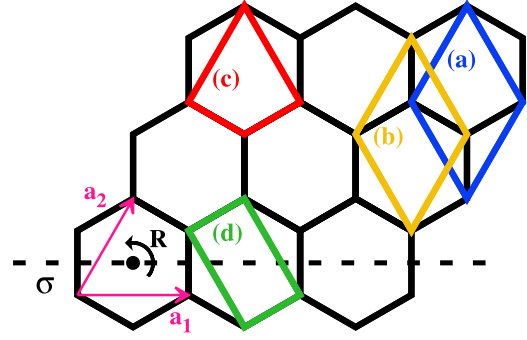

FIG. 12. Symmetry generators of the point group of the honeycomb lattice (σ and R). As an example, we show the loops for which we computed the SU(2) flux: (a) parallelogram-shaped (sublattice A), (b) parallelogram-shaped (sublattice B), (c) diamond, and (d) rectangular plaquettes.

Table I) is given by

$$g(j) = (-i\sigma_3)^s \exp\left[i\frac{\pi}{12}\sigma_3\right] \exp\left[-i\frac{2\pi}{3}(n_j - m_j)\sigma_3\right].$$
(A6)

In our gauge the *Ansatz* matrix reads

$$u_{ij} = \begin{cases} t\sigma_3 \exp[i\phi_{ij}\sigma_3], & (i,j) \text{ first neighbor,} \\ \Delta\sigma_1 \exp[i\theta_{ij}\sigma_3], & (i,j) \text{ second neighbor,} \end{cases}$$
(A7)

where the phases ϕ_{ij} and θ_{ij} are the ones in Fig. 3.

To conclude, let us discuss the gauge-invariant fluxes of the $d \pm id$ state on the honeycomb lattice. For any lattice loop $\mathcal{C}$ with base site j, we can define the SU(2) flux

$$P_j = \prod_{\mathcal{C}} u_{kl} = u_{jj_2} u_{j_2 j_3} \cdots u_{j_p j},$$
(A8)

where p is the number of sites in the loop. The trace of the 2×2 matrix P_j is independent of the base site j [44],

$$\text{Tr } P_j = \begin{cases} 2\rho \cos(\theta), & p \text{ even,} \\ 2i\rho \sin(\theta), & p \text{ odd,} \end{cases}$$
(A9)

and the angle θ is the gauge-invariant quantity that characterizes the SU(2) gauge flux.

For the $d \pm id$ *Ansatz*, pure first-neighbor loops have trivial fluxes ($\theta = 0$) since the first-neighbor hopping is gauge equivalent to the uRVB state. The second-neighbor pairings, however, have nontrivial SU(2) flux with $\theta = \pm 2\pi/3$ through the parallelogram-shaped plaquettes of the triangular sublattices A [Fig. 12, loop (a)] and B [Fig. 12, loop (b)]. Odd-site loops do not contain nontrivial flux since the state is time reversal invariant. As far as loops made from two first-neighbor and two second-neighbor links are concerned, we can have either a diamond $J_1 J_1 J_2 J_2$ [Fig. 12, loop (c)] or a rectangular $J_1 J_2 J_1 J_2$ [Fig. 12, loop (d)] plaquette. In the $d \pm id$ state, the trace of flux through the diamond plaquettes is trivial, while it gives $\theta = \pi$ through the rectangular plaquettes. These gauge-invariant fluxes are related to expectation values of certain multiple-spin operators [44].

[1] C. Lacroix, P. Mendels, and F. Mila, *Introduction to Frustrated Magnetism: Materials, Experiments, Theory*, Springer Series in Solid-State Sciences (Springer, New York, 2011), Vol. 164.

[2] H.-C. Jiang, H. Yao, and L. Balents, Phys. Rev. B **86**, 024424 (2012).

[3] W.-J. Hu, F. Becca, A. Parola, and S. Sorella, Phys. Rev. B **88**, 060402 (2013).

[4] L. Wang, D. Poilblanc, Z.-C. Gu, X.-G. Wen, and F. Verstraete, Phys. Rev. Lett. **111**, 037202 (2013).

[5] S.-S. Gong, W. Zhu, D. N. Sheng, O. I. Motrunich, and M. P. A. Fisher, Phys. Rev. Lett. **113**, 027201 (2014).

[6] D. Poilblanc and M. Mambrini, Phys. Rev. B **96**, 014414 (2017).

[7] R. V. Mishmash, J. R. Garrison, S. Bieri, and C. Xu, Phys. Rev. Lett. **111**, 157203 (2013).

[8] R. Kaneko, S. Morita, and M. Imada, J. Phys. Soc. Jpn. **83**, 093707 (2014).

[9] Z. Zhu and S. R. White, Phys. Rev. B **92**, 041105 (2015).

[10] W.-J. Hu, S.-S. Gong, W. Zhu, and D. N. Sheng, Phys. Rev. B **92**, 140403 (2015).

[11] Y. Iqbal, W.-J. Hu, R. Thomale, D. Poilblanc, and F. Becca, Phys. Rev. B **93**, 144411 (2016).

[12] S. Yan, D. A. Huse, and S. R. White, Science **332**, 1173 (2011).

[13] S. Depenbrock, I. P. McCulloch, and U. Schollwöck, Phys. Rev. Lett. **109**, 067201 (2012).

[14] Y. Iqbal, F. Becca, S. Sorella, and D. Poilblanc, Phys. Rev. B **87**, 060405 (2013).

[15] Y.-C. He, M. P. Zaletel, M. Oshikawa, and F. Pollmann, Phys. Rev. X **7**, 031020 (2017).

[16] H. J. Liao, Z. Y. Xie, J. Chen, Z. Y. Liu, H. D. Xie, R. Z. Huang, B. Normand, and T. Xiang, Phys. Rev. Lett. **118**, 137202 (2017).

[17] E. H. Lieb, T. Schultz, and D. J. Mattis, Ann. Phys. (N.Y.) **16**, 407 (1961).

[18] I. Affleck, Phys. Rev. B **37**, 5186 (1988).

[19] M. Oshikawa, Phys. Rev. Lett. **84**, 1535 (2000).

[20] G. Misguich, C. Lhuillier, M. Mambrini, and P. Sindzingre, Eur. Phys. J. B **26**, 167 (2002).

[21] M. B. Hastings, Phys. Rev. B **69**, 104431 (2004).

[22] E. Rastelli, A. Tassi, and L. Reatto, Phys. B (Amsterdam, Neth.) **97**, 1 (1979).

[23] J.-B. Fouet, P. Sindzingre, and C. Lhuillier, Eur. Phys. J. B **20**, 241 (2001).

[24] A. Mulder, R. Ganesh, L. Capriotti, and A. Paramekanti, Phys. Rev. B **81**, 214419 (2010).

[25] F. Wang, Phys. Rev. B **82**, 024419 (2010).

[26] Y. M. Lu and Y. Ran, Phys. Rev. B **84**, 024420 (2011).

[27] B. K. Clark, D. A. Abanin, and S. L. Sondhi, Phys. Rev. Lett. **107**, 087204 (2011).

[28] F. Mezzacapo and M. Boninsegni, Phys. Rev. B **85**, 060402 (2012).

[29] A. Di Ciolo, J. Carrasquilla, F. Becca, M. Rigol, and V. Galitski, Phys. Rev. B **89**, 094413 (2014).

[30] R. F. Bishop, P. H. Y. Li, and C. E. Campbell, J. Phys. Condens. Matter **25**, 306002 (2013).

[31] J. Reuther, D. A. Abanin, and R. Thomale, Phys. Rev. B **84**, 014417 (2011).

[32] J. Oitmaa and R. R. P. Singh, Phys. Rev. B **84**, 094424 (2011).

[33] H. Mosadeq, F. Shabazi, and S. A. Jafary, J. Phys. Condens. Matter **23**, 226006 (2011).

[34] A. F. Albuquerque, D. Schwandt, B. Hetenyi, S. Capponi, M. Mambrini, and A. M. Läuchli, Phys. Rev. B **84**, 024406 (2011).

[35] Z. Zhu, D. A. Huse, and S. R. White, Phys. Rev. Lett. **110**, 127205 (2013).

[36] S.-S. Gong, D. N. Sheng, O. I. Motrunich, and M. P. A. Fisher, Phys. Rev. B **88**, 165138 (2013).

[37] R. Ganesh, S. Nishimoto, and J. van den Brink, Phys. Rev. B **87**, 054413 (2013).

[38] R. Ganesh, J. van den Brink, and S. Nishimoto, Phys. Rev. Lett. **110**, 127203 (2013).

[39] R. Flint and P. A. Lee, Phys. Rev. Lett. **111**, 217201 (2013).

[40] Z. Y. Meng, T. C. Lang, S. Wessel, F. F. Assaad, and A. Muramatsu, Nature (London) **464**, 847 (2010).

[41] S. Sorella, Y. Otsuka, and S. Yunoki, Sci. Rep. **2**, 992 (2012).

[42] E. Manousakis, Rev. Mod. Phys. **63**, 1 (1991).

[43] X.-G. Wen, Phys. Rev. B **65**, 165113 (2002).

[44] S. Bieri, C. Lhuillier, and L. Messio, Phys. Rev. B **93**, 094437 (2016).

[45] Y. Iqbal, F. Becca, and D. Poilblanc, New J. Phys. **14**, 115031 (2012).

[46] S. Sorella, Phys. Rev. B **71**, 241103 (2005).

[47] E. V. Castro, N. M. R. Peres, K. S. D. Beach, and A. W. Sandvik, Phys. Rev. B **73**, 054422 (2006).

[48] P. Chandra, P. Coleman, and A. I. Larkin, Phys. Rev. Lett. **64**, 88 (1990).

[49] T. Senthil, A. Vishwanath, L. Balents, S. Sachdev, and M. P. A. Fisher, Science **303**, 1490 (2004).

[50] T. Senthil, L. Balents, S. Sachdev, A. Vishwanath, and M. P. A. Fisher, Phys. Rev. B **70**, 144407 (2004).

[51] S. Pujari, F. Alet, and K. Damle, Phys. Rev. B **91**, 104411 (2015).

[52] K. Harada, Phys. Rev. E **84**, 056704 (2011); **92**, 012106 (2015).

[53] R. K. Kaul, R. G. Melko, and A. W. Sandvik, Annu. Rev. Condens. Matter Phys. **4**, 179 (2013).